JOURNAL OF MATERIALS SCIENCE 27 (1992) 3286–3292

Structural studies of amorphous Zn–P films

P. LECANTE, A. MOSSET, J. GALY
CEMES-LOE/CNRS, 29, rue Jeanne Marvig, BP 4347, 31055 Toulouse Cedex, France
A. BURIAN
Zaklad Fizyki Ciala Stalego PAN, Kawalca 3, 41800 Zabrze, Poland

Large angle X-ray diffraction studies were performed on vapour deposited Zn–P amorphous films with phosphorus contents of 43, 50 and 68 at %. Using Mo$K\alpha$ radiation, measurements have been made for $4\pi \sin\theta/\lambda$ between 0.06 and 1.6 nm^{-1}. The experimental method and data reduction procedure are described. The structure of the amorphous Zn–P films is analysed using both intensity and radial distribution functions. The experimental results are compared with a number of paracrystalline models based on various crystalline polymorphs of the II–V system. Comparison shows that reasonable agreement is achieved for distorted tetrahedral structures: the intermediate between CdAs and Si type III for $Zn_{57}P_{43}$ and $Zn_{50}P_{50}$ and the distorted $CdAs_2$ for $Zn_{32}P_{68}$. The sizes of the microparacrystals are evaluated from the integral widths of the first diffraction peaks and the lattice distortions by applying paracrystalline theory. It is shown that the size of the microparacrystal and the degree of the lattice distortion are correlated by the α^* relation for the investigated Zn–P amorphous films.

1. Introduction

In the binary semiconducting Zn–P system, three crystalline phases (Zn_3P_2, α- and β-ZnP_2) were revealed [1]. Most previous investigations have concentrated on Zn_3P_2 single crystal and polycrystalline thin films [2–7]. Optical and electrical properties, i.e. the existence of the optical direct transition at 1.5 eV with a high absorption coefficient (greater than 10^4 cm^{-1}), make these attractive as the active layer in solar cells [8–11]. Solar cells with efficiency of 6 and 2% for the crystalline bulk material and the thin films, respectively, were reported. The Zn–P system is characterized by its ability to form amorphous films when the polycrystalline Zn_3P_2 material is evaporated and deposited in vacuum onto a substrate at room temperature. Although the preparation and characterization of a-Zn_3P_2 films are reported in the literature [12–18] together with their optical and electrical properties, their atomic structure has not been studied. In this paper, X-ray diffraction (XRD) structural studies of the amorphous Zn–P films with phosphorus contents of 43, 50 and 68 at %, prepared by vacuum evaporation, are presented.

2. Experimental procedure

2.1. Sample preparation

The amorphous films of zinc phosphide were prepared by thermal evaporation of bulk polycrystalline Zn_3P_2 and α-ZnP_2 materials onto glass substrates maintained at room temperature. The substrates were cleaned ultrasonically in absolute ethanol. The evaporation was performed at a pressure of 1.333×10^{-3} Pa. The source material was evaporated from a corundum crucible resistively heated with a tantalum spiral. Chemical analysis showed that the composition of the films prepared from the Zn_3P_2 source material were $Zn_{57}P_{43}$ and $Zn_{50}P_{50}$ at deposition rates of 10 and 30 $nm\,s^{-1}$, respectively. The films obtained by evaporation of ZnP_2 at a deposition rate of 5 $nm\,s^{-1}$ contained 68 at % P ($Zn_{32}P_{68}$). The final film thicknesses of 35, 50 and 16 μm were achieved for compositions at 43, 50 and 68 at % P using a series of 5-min evaporation runs. The densities of the amorphous films were calculated from direct thickness, area and weight measurements. The determined density values were 3.65, 3.41 and 3.50 $g\,cm^{-3}$ for $Zn_{57}P_{43}$, $Zn_{50}P_{50}$ and $Zn_{32}P_{68}$.

2.2. Large-angle XRD measurements

The XRD data were collected using a diffractometer attached with a position-sensitive detector, a molybdenum target tube, a flat graphite monochromator mounted in the primary beam and an evacuated chamber before the detector. A detailed description of the diffractometer is given elsewhere [19]. The measurements were performed in a symmetrical transmission geometry [20–22]. The data were collected from $k = 0.06$ to 1.6 nm^{-1} ($k = 4\pi \sin\theta/\lambda$ where 2θ is the scattering angle and λ is the wavelength of the X-ray radiation).

3. Data processing

The use of the position-sensitive detector in the diffractometer allows collection of the intensities within a short period [19]. A main disadvantage of the diffractometer with the incident-beam monochromator is that fluorescence radiation, possibly

0022–2461

excited in a sample, is recorded by the detector. $I'_m = I_m + I_{f,m}$ where I'_m and I_m indicate the measured intensity with and without the detected fluorescence $I_{f,m}$. This extra radiation, which cannot be eliminated by the position-sensitive detector and its associated electronics, leads to serious problems with correction and normalization of the data. In Fig. 1, the Zn fluorescent intensity measured from the $Zn_{32}P_{68}$ amorphous film is shown. The correction factor for absorption and variation of irradiated volume for a flat, extended sample can be written for the symmetrical transmission geometry [23] as

$$A_f(\theta) = \exp(-\mu_f t/\cos\theta)\frac{\exp(\Delta\mu t/\cos\theta) - 1}{\Delta\mu} \quad (1)$$

where $\Delta\mu = \mu_f - \mu$, μ_f and μ are the linear absorption coefficients for the fluorescent and incident radiation respectively, and t is the sample thickness. On the other hand, the fluorescent intensity can be calculated from Equation 1 by multiplying $A_f(\theta)$ by a constant I_f° as $I_f = A_f(\theta)\, I_f^\circ$. μ_f has been evaluated from tabulated values of the mass absorption coefficients, assuming the intensity ratio of the $K_{\alpha 1}:K_{\alpha 2}:K_\beta$ contributions to be 1:0.5:0.2 [24]. The calculated curve is shown in Fig. 1, and is identical to the experimental one. In this figure the resultant fluorescent intensity, after correction according to Equation 1, is also presented. It can be seen that I_f/A_f is independent of angle to within the counting statistics. According to North and Wagner [20] such a measurement can be used as a test of alignment of the apparatus. Assuming that the amount of the fluorescence recorded by the detector system $I_{f,m}$ is proportional to the measured (or calculated) fluorescent intensity $I_{f,m} = bI_f$, the scaling factor b was obtained as follows. In our previous paper [25], it was shown that the correction term for absorption and change of irradiated volume, usually applied in the case of a point detector [23]

$$A(\theta) = t/\cos\theta \exp(-\mu t/\cos\theta), \quad (2)$$

is valid for the linear position-sensitive detector used in a scanning mode. The intensity scattered by non-crystalline materials, corrected for absorption, irradiated volume and polarization, oscillates weakly around the independent intensity I_{ind} in the region of high angles and finally approaches I_{ind}.

$$I_{ind} = 1/N_a \sum_{p=1}^{N_a} |f_p|^2 + R(A'/A) I_p^{Comp} \quad (3)$$

where f_p is the atomic scattering factor for the pth atom appropriately corrected for the anomalous dispersion [26–28], I_p^{Comp} is the Compton intensity, R is the recoil factor [29], (A'/A) is the term resulting from increased absorption of the Compton intensity [21], and N_a is the number of atoms. The normalization constant, c_{nor}, is calculated as the quotient

$$c_{nor} = I_{ind}/I_c \quad (4)$$

averaged over the oscillation free region. $I_c = I_m/(PA)$ where I_m is the measured intensity and P is the polarization factor [23]. The double scattering should be considered and subtracted if necessary from the experimental intensity in the case of samples with low absorption coefficients [29–32]. The double scattering, calculated using the tables given by Dwiggins [30], was about 2.5% of the total intensity for the investigated films. Inserting Equation 2 into Equation 4

$$\ln\left(\frac{I_m \cos\theta}{PI_{ind}}\right) = -\frac{\mu t}{\cos\theta} - \ln\left(\frac{c_{nor}}{t}\right) \quad (5)$$

Plotting $\ln(I_m \cos\theta/PI_{ind})$ against $1/\cos\theta$, we find that this function oscillates about a straight line for the experimental data free from the spurious details. The measured fluorescence multiplied by the scaling factor b was subtracted from the experimental intensity $I_m = I'_m - bI_f$. The linear behaviour of the plot described by Equation 5 was a criterion for the appropriate choice of the scaling factor. For the $Zn_{57}P_{43}$ and $Zn_{50}P_{50}$ films, this procedure was applied with the calculated fluorescence contribution. The corresponding plots are shown in Fig. 2. Such corrected experimental data were subjected to the standard procedure of correction for absorption, polarization and normalization [33, 34]. The resulting intensities together with I_{ind} are shown in Fig. 3. On the basis of the plots presented in Fig. 2, the values of μt calculated from the tabulated absorption coefficients and the measured thicknesses of the samples could be verified within a few per cent. In Table I, the values of μt both calculated and determined using the present method, are shown.

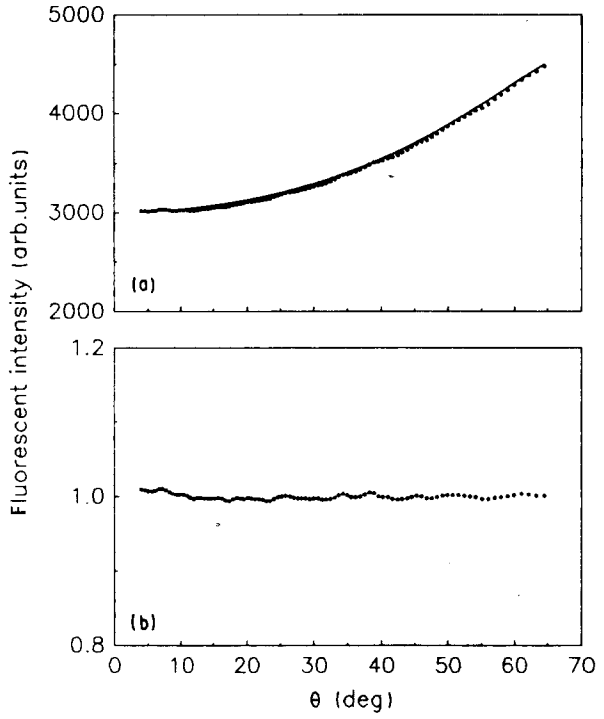

Figure 1 Fluorescent intensity for the $Zn_{32}P_{68}$ amorphous film. (a) (. . .) measured; (—) calculated; (b) corrected for absorption and change of irradiated volume.

4. Results and discussion

The interpretation of the experimental data has been performed by comparison of both experimental intensity $k\,i(k)$ and radial distribution $4\pi r(\rho - \rho_0)$ functions with microparacrystalline calculations. These

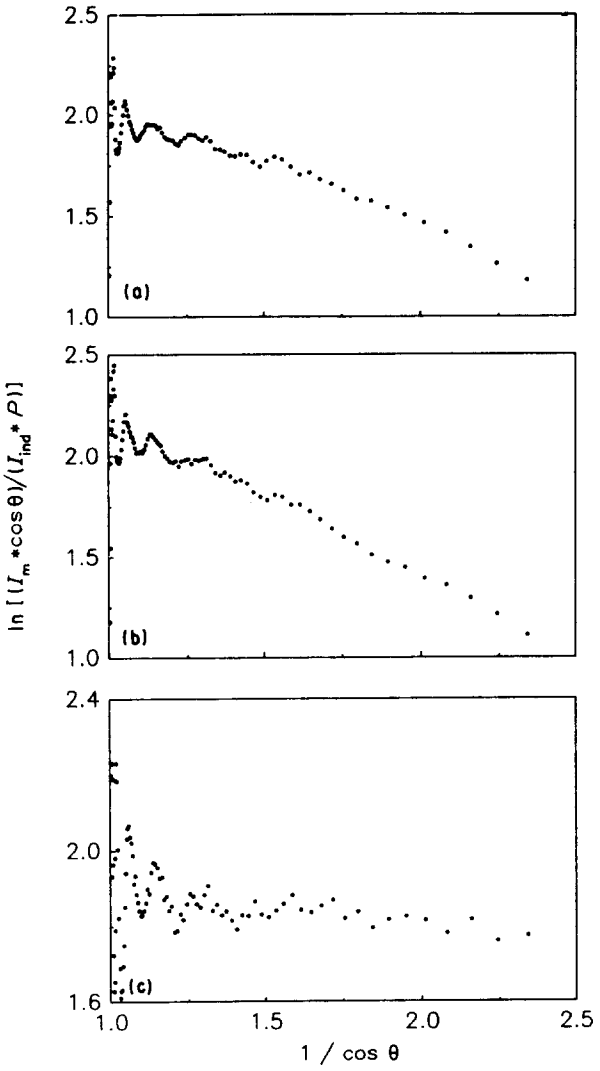

Figure 2 Plots of $\ln(I_m \cos\theta / PI_{ind})$ against $1/\cos\theta$. (a) $Zn_{57}P_{43}$; (b) $Zn_{50}P_{50}$; (c) $Zn_{32}P_{68}$.

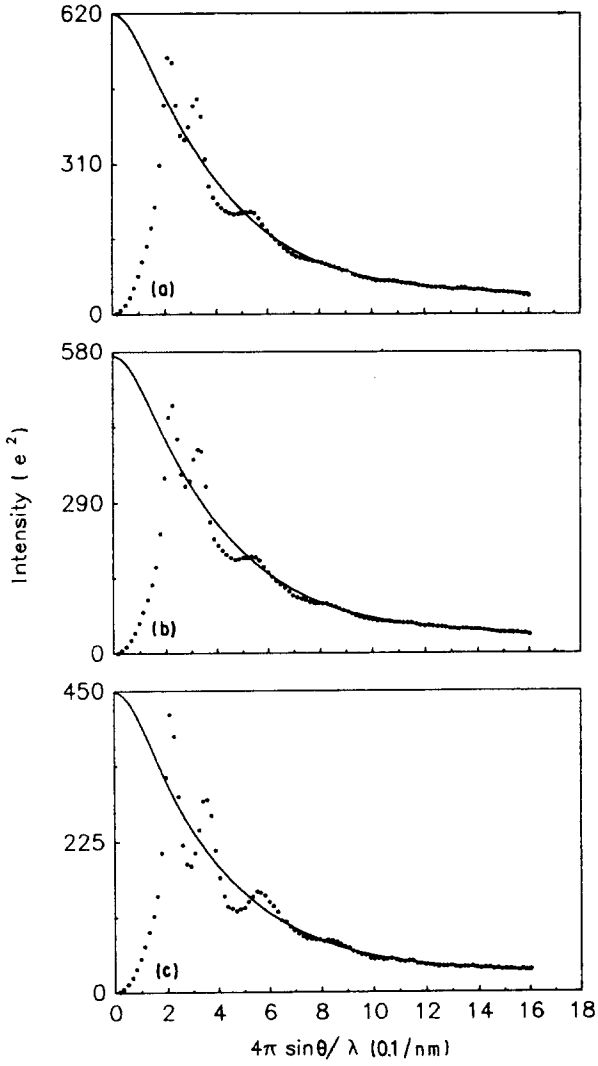

Figure 3 Corrected and normalized intensities together with independent scattering. (a) $Zn_{57}P_{43}$; (b) $Zn_{50}P_{50}$; (c) $Zn_{32}P_{68}$.

functions are related as follows:

$$4\pi r(\rho - \rho_0) = \frac{2}{\pi}\int_0^{k_{max}} k\, i(k)\, M(k) \sin(kr)\, dk \qquad (6)$$

where $i(k) = I - I_{ind}$, I is the intensity corrected for absorption and polarization expressed in electron units.

$$M(k) = \left(\left| \sum_{p=1}^{N_a} f_p(0) \right|^2 \Big/ \left| \sum_{p=1}^{N_a} f_p(k) \right|^2 \right) \exp(-0.015k^2)$$

Assuming three-dimensional Gaussian distribution of interatomic distances r_{pq}, the $4\pi r^2\rho(r)$ function averaged over all orientations may be written as [35, 40–42]

$$4\pi r^2 \rho(r) = r \frac{1}{N_a} \sum_{\substack{p=1 \\ p\neq q}}^{N_a} \sum_{q=1}^{N_a} \int_0^{\infty} \frac{1}{(2\pi\sigma_{pq}^2)^{1/2}} \frac{1}{r_{pq}}$$
$$\{\exp[-(r' - r_{pq})^2/2\sigma_{pq}^2] - \exp[-(r' + r_{pq})^2/2\sigma_{pq}^2]\}$$
$$[P_{pq}(r - r') - P_{pq}(r + r')]\, dr' \qquad (7)$$

where $r_{pq} = |r_{pq}|$, σ_{pq} is the standard deviation of the atom p atom q distance.

$$P_{pq}(r) = \frac{1}{\pi}\int_0^{k_{max}} f_p f_q^*\, M(k) \cos(kr)\, dk$$

TABLE I Values of the μt product determined from tabulated absorption coefficients (calculated) and from Equation 5 (present method).

Sample	μt (Calculated)	μt (present method)
$Zn_{57}P_{43}$	0.546	0.560
$Zn_{50}P_{50}$	0.754	0.790
$Zn_{32}P_{68}$	0.175	0.160

The theoretical intensity function $k\, i_{th}(k)$ is expressed as

$$k i_{th}(k) = \frac{1}{N_a} \sum_{\substack{p=1 \\ p\neq q}}^{N_a} \sum_{q=1}^{N_a} f_p f_q^* \frac{\sin(kr_{pq})}{r_{pq}}$$
$$\times \exp(-k^2\sigma_{pq}^2/2) - k i_0(k) \qquad (8)$$

where $i_0(k)$ is the small-angle Debye scattering, and * indicates the complex conjugate.

The theoretical radial distribution function is calculated from $k\, i_{th}(k)$ according to Equation 6 under the same conditions as in the experiment. The standard deviations σ_{pq} are assumed to be adjustable parameters. The unwanted $k i_0(k)$ contribution may be subtracted using the procedure described by Michell [36]. From the paracrystalline approach to the structure of disordered systems, it follows that the size of

the paracrystal expressed by the mean number of the net planes $\langle N \rangle + 1$ and the distortion of the lattice described by the relative standard deviation of the interplanar distance $g = [(\langle d^2 \rangle - \langle d \rangle^2)/\langle d \rangle^2]^{1/2}$ are correlated by the α^* relation [37, 38]

$$\langle N \rangle^{1/2} g = \alpha^*, \quad 0.1 \leq \alpha^* \leq 0.2 \tag{9}$$

For the paracrystals, the integral width of the diffraction profile $\delta s (s = 2 \sin \theta / \lambda)$ for first order reflection is expressed by the following equation:

$$\delta s = \frac{1}{\langle d \rangle} \left[\frac{1}{\langle N \rangle} + (\pi g)^2 \right], \tag{10}$$

from which $\langle N \rangle$ can be calculated.

4.1. Structural model for $Zn_{57}P_{43}$ and $Zn_{50}P_{50}$ amorphous films

The experimental intensity $ki(k)$ and $4\pi r(\rho - \rho_0)$ functions for the amorphous films of composition $Zn_{57}P_{43}$ and $Zn_{50}P_{50}$ are similar (Fig. 4). Attempts have been made to simulate their atomic structure based on the crystalline Zn_3P_2 model containing 40 atoms [39] with $\sigma = 0.03$ for the near neighbours and 0.2 for remaining interatomic distances. The comparison of the experimental and calculated functions is shown in Fig. 4, and it is seen that the model based on the Zn_3P_2 structure is inadequate to account for the experimental data.

The crystalline structure of the Zn_3P_2 structure is of the antifluorite type, in which P atoms form the distorted f c c lattice and Zn atoms occupy six tetrahedral voids. The experimental intensity and radial distribution functions cannot be fitted by this model. Moreover, mesomeric (or resonance) bonding, typical for crystalline Zn_3P_2 [39], is not expected to be the case for amorphous materials [40, 41]. A good fit is obtained using the model based on the hypothetical 1:1 structure, intermediate between cubic Si III [42] and orthorhombic CdAs [43]. It has previously been shown [35] that this structure is adequate to account for the experimental data obtained for the Cd–As amorphous films. The structural parameters of the model consisting of 40 atoms packed inside the {2 1 1} orthorhombic bipyramide are given in Table II. In the hypothetical ZnP structure, the Zn atoms are coordinated by 3 P and 1 Zn, each P atom having 3 Zn and 1 P as nearest neighbours. Thus the Zn–P, Zn–Zn and P–P contributions are involved in the first peak of the radial distribution function. The difference between the chemical composition of the $Zn_{57}P_{43}$

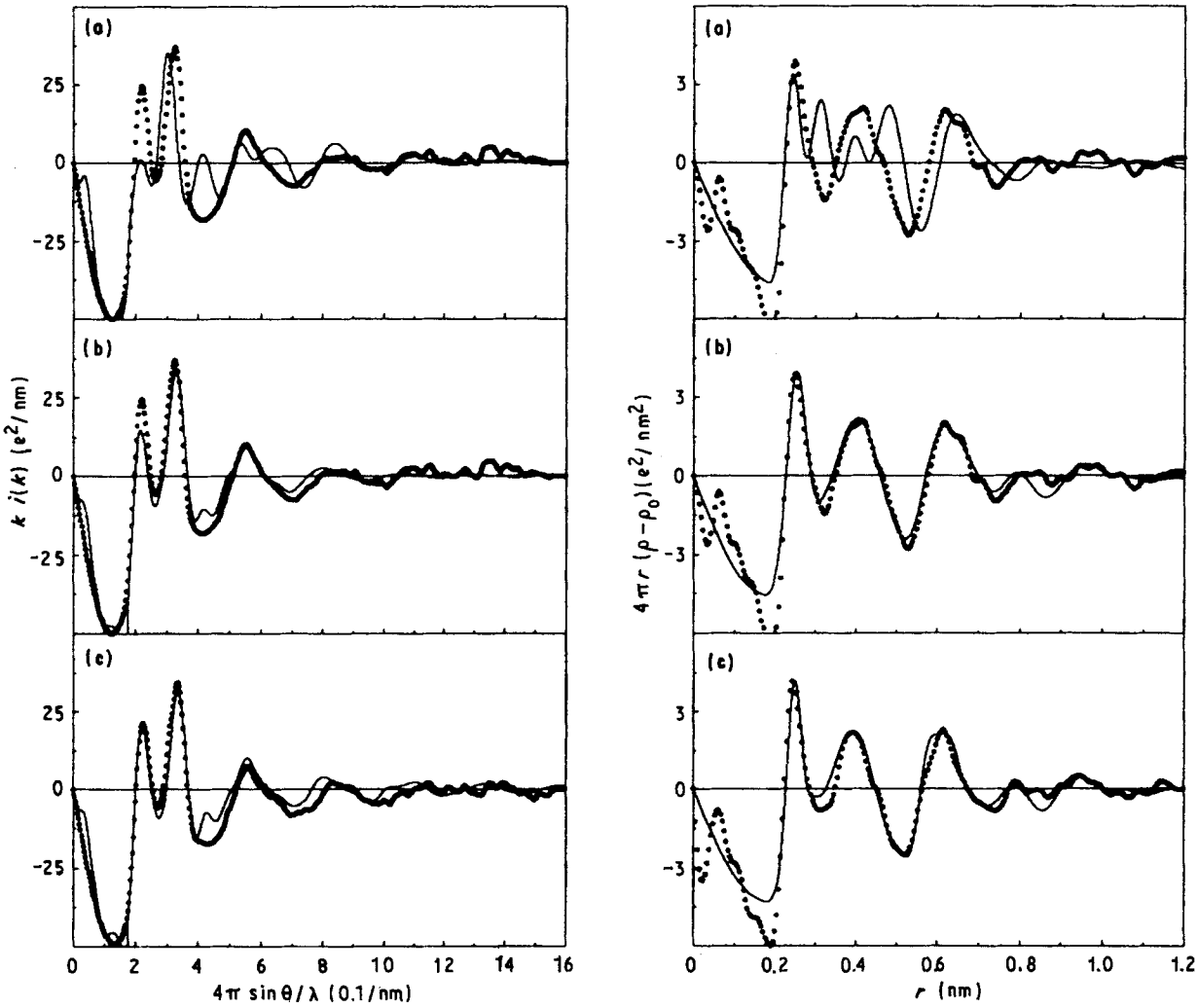

Figure 4 Experimental and calculated reduced intensities (left) and differential radial distribution functions (right) for Zn-rich amorphous films. (a) . . . , $Zn_{57}P_{43}$ experimental function; —, Zn_3P_2 model function; (b) . . . $Zn_{57}P_{43}$ experimental; —, ZnP model; (c) . . . $Zn_{50}P_{50}$ experimental; —, ZnP model.

sample and 1:1 stoichiometry has been taken into account, allowing the P positions to be statistically occupied.

4.2. Structural models for $Zn_{32}P_{68}$ amorphous film

Similar calculations to those for the Zn-rich samples were made for the $Zn_{32}P_{68}$ amorphous film. The structures of the crystalline polymorphs α- and β-ZnP_2 were considered as the models for the phosphorus-rich film. A comparison of the experimental and calculated curves presented in Fig. 5 shows that the short-range order, i.e. the order containing first- and second-neighbour interatomic distances (up to about 0.4 nm) is well modelled by these structures, but poor agreement with experiment is seen for $r > 0.4$ nm. For the α-ZnP_2 model, the near-neighbours σ value was 0.03; for $r = 0.352$–0.433 nm, $\sigma = 0.27$; $r = 0.455$–0.505 nm, $\sigma = 0.5$; $r = 0.508$, $\sigma = 0.75$; $r > 0.509$, $\sigma = 0.35$. The parameters of the β-ZnP_2 model were as follows: for the near neighbours $\sigma = 0.1$; for $r = 0.341$–0.366 nm, $\sigma = 0.12$; $r = 0.37$–0.393 nm, $\sigma = 0.17$; $r = 0.401$–0.697 nm, $\sigma = 0.2$; and for $r > 0.7$ nm, $\sigma = 0.3$. The third radial distribution peak at about 0.6 nm is better reproduced by the model based on the $CdAs_2$ structure [44, 45], which also satisfactorily describes the atomic arrangement in the arsenic-rich Cd–As amorphous films [35]. These three structures have common characteristics—their lattices are formed by a corner-sharing distorted

TABLE II Model parameters of hypothetical ZnP structure for $Zn_{57}P_{43}$ and $Zn_{50}P_{50}$ amorphous films.

$Zn_{57}P_{43}$		$Zn_{50}P_{50}$	
Interatomic distance (nm)	σ	Interatomic distance (nm)	σ
r_{P-P} 0.219	0.030	0.220	0.025
r_{Zn-P} 0.250	0.120	0.247	0.025
r_{Zn-Zn} 0.280	0.150	0.289	0.100
0.353–0.395	0.700	0.343–0.357	0.750
0.412–0.431	0.500	0.388–0.427	0.600
0.513–0.596	0.300	0.514–0.640	0.150
0.602–0.696	0.270	0.651–	0.30
0.703–0.800	0.300		
0.808–	0.350		

Space group $P\bar{a}3$	$Zn_{57}P_{43}$(nm)	$Zn_{50}P_{50}$(nm)
	$a = 0.6955$	0.6900
Cd in 8(c):(x, x, x)	$x = 0.616$	0.621
As in 8(c):(x, x, x)	$x = 0.091$	0.092

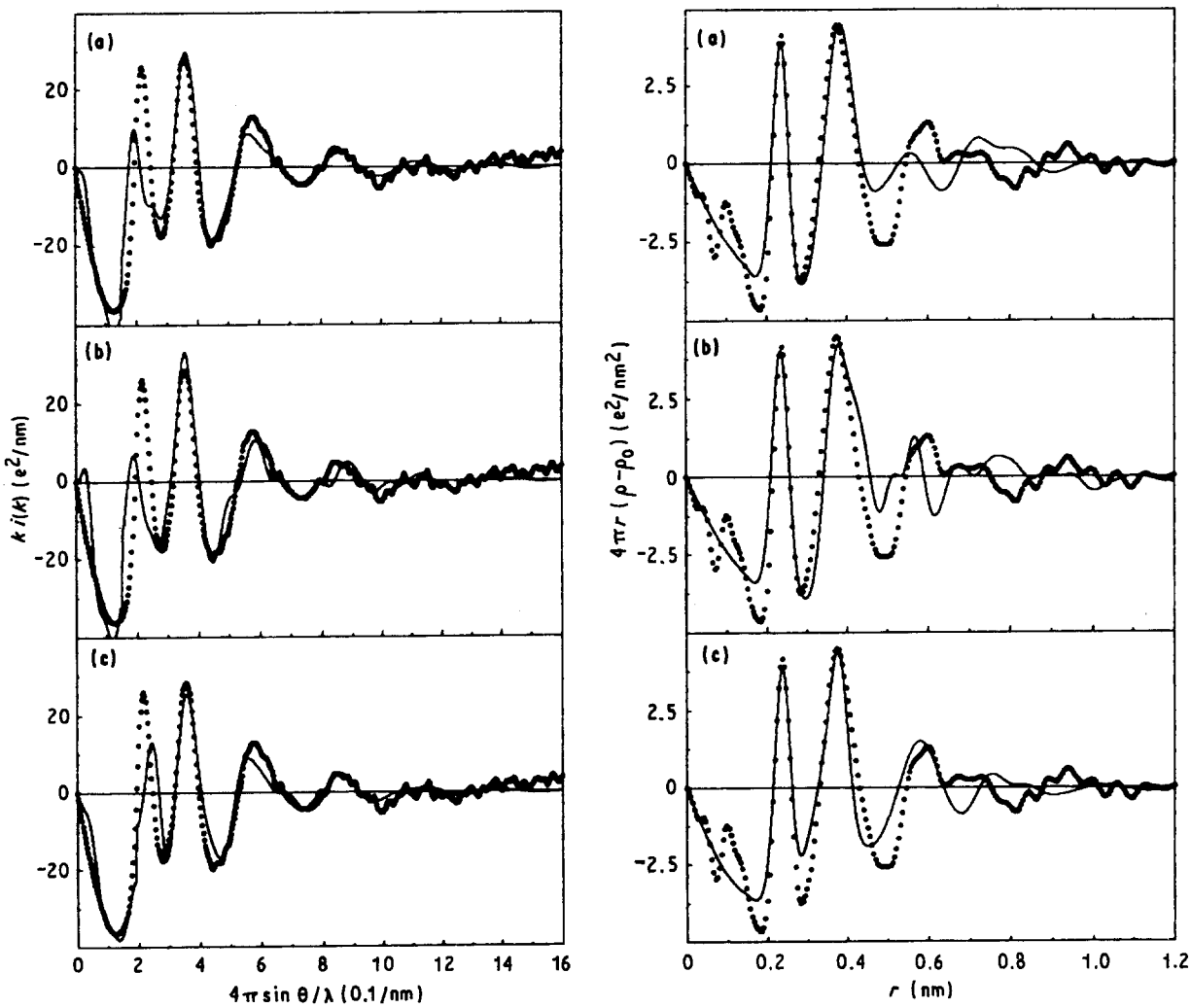

Figure 5 Experimental and calculated reduced intensities (left) and differential radial distribution functions (right) for the $Zn_{32}P_{68}$ amorphous film. . . . , $Zn_{32}P_{68}$ experimental function. —, (a) α-ZnP_2; (b) β-ZnP_2; (c) $CdAs_2$ model functions.

tetrahedra arrangement. In the α-ZnP_2 and $CdAs_2$ structures, the Zn (Cd) atom is coordinated by four P (As) atoms, and each P (As) atom has two Zn (Cd) and two P (As) atoms as nearest neighbours. In the β-ZnP_2 type, one half of Zn atoms are bounded to 4 P and the other half to 1 Zn and 3 P atoms. Three from four independent P atoms are bounded to 2 Zn and 2 P, the fourth P atom being bounded to 1 Zn and 3 P. The crystalline lattice of $CdAs_2$ has been scaled to simulate the macroscopic density of 3.5 g cm^{-3}. Moreover, the ZnP_4 tetrahedra have been contracted along the bond Zn–P axis by 0.015 nm to reproduce the near-neighbour distances. This deformation leads to dispersion of the Zn–P and P–P bond lengths which is characteristic for α- and β-ZnP_2 structures [46, 47] as well as deformation in the spiral chains formed by the P atoms. The model parameters are listed in Table III. The curves shown in Fig. 5 are calculated on the basis of the $CdAs_2$ model containing 30 atoms packed into the {2 1 1} tetragonal trapezohedron. This model gives better match to experiment than those of α- and β-ZnP_2.

4.3. α* relation for amorphous Zn–P films

The integral width of the first and most intense diffraction peaks were determined by decomposing the diffraction intensity in the range of 0–0.8 nm on three overlapping Lorentzians [48]. δs (see Equation 10) was then evaluated. The paracrystalline distortion parameter g was estimated from the model distortions as the average value of the standard deviations of the interatomic distances between atoms which occupy the neighbouring net planes divided by $\langle d \rangle$ [35, 49]. From the theory of paracrystals it follows that the 'bearing net planes', i.e. the most densely packed net planes, should be taken into account when analysing the α* relation [38]. These net planes also limit the volume of the paracrystals. $\langle N \rangle$ can be obtained according to Equation 10. Table IV includes the values of δs, g and $\langle N \rangle$ together with $\langle N \rangle^{1/2} g$, and shows that the α* relation is satisfied for the investigated amorphous Zn–P films.

TABLE III Model parameters for $Zn_{32}P_{68}$ amorphous film based on $CdAs_2$ structure.

Interatomic distance (nm)			σ
r_{P-P}	0.211 0.222 0.233	$\langle r_{P-P} \rangle = 0.223$	0.02
r_{Zn-P}	0.233 0.235 0.239 0.246 0.256	$\langle r_{Zn-P} \rangle = 0.241$	0.02
	0.322 – 0.345		0.25
	0.359 – 0.432		0.15
	0.451 – 0.529		0.25
	0.550 – 0.691		0.35
	0.728 –		0.30

Space group $I\,4_122$ $a = 0.742$ nm $c = 0.432$ nm
Zn in 4(*d*):(0, 0, 0) P in 8(*f*):(*x*, 1/4, 1/8) with $x = 0.434$

TABLE IV Values of δs, g, $\langle N \rangle$ and $\langle N \rangle^{1/2} g$.

	δs	g	$\langle N \rangle$	$\langle N \rangle^{1/2} g$
$Zn_{57}P_{43}$	0.17	0.11	$2.75 \approx 3$	0.19
$Zn_{50}P_{50}$	0.17	0.11	$2.78 \approx 3$	0.19
$Zn_{32}P_{68}$	0.19	0.12	$2.77 \approx 3$	0.20

It is noteworthy that the α* relation limits the size of the models. For a larger model, the use of the calculation procedure presented here produces too much structure in the high r region of the radial distribution function. Therefore the higher values of σ and hence g should be taken into account for the experimental data. However, for the large $\langle N \rangle$ value, the paracrystalline distortion parameter g cannot increase without limitations, as follows from Equation 9. The extents of the constructed models of about 0.9 nm are in agreement with the estimations obtained from the paracrystalline theory. The $\langle N \rangle$ and g values collected in Table IV indicate that the description of the Zn–P amorphous structures is at the limit of applicability of the paracrystalline approach. For lower $\langle N \rangle$ and greater g, the network cannot be paracrystalline—the structure should be considered rather in terms of the random network model.

5. Summary

The XRD data for the amorphous Zn–P films are interpreted in terms of the paracrystalline approach. Two structural models, one intermediate between Si III and CdAs type, and the second based on $CdAs_2$ lattice, are adequate to account for the experimental data in the Zn- and P-rich compositional regions, respectively. Comparison with previously studied amorphous cadmium arsenide films shows that there is a correspondence between the atomic arrangement in Zn–P and Cd–As amorphous films. From analysis of the diffraction profile, it is found that the α* relation with $\langle N \rangle^{1/2}\ g = 0.19$–$0.20$ is satisfied for the zinc phosphide amorphous films investigated.

References

1. W. ZDANOWICZ and L. ZDANOWICZ, in *Ann. Rev. Mater. Sci.* **5** (1975) 301.
2. E. A. FAGEN, *J. Appl. Phys.* **50** (1979) 6505.
3. J. M. PAWLIKOWSKI, J. MISIEWICZ and N. MIROWSKA, *J. Phys. Chem. Solids* **40** (1979) 1027.
4. V. V. SOBOLEV and N. N. SYRBU, *Phys. Status Solidi* **B64** (1974) 423.
5. A. CATALANO, *J. Crystal Growth* **49** (1980) 681.
6. K. KLOC and W. ZDANOWICZ, *ibid.* **66** (1984) 451.
7. T. IWAMI, S. FUKE, S. KAWARABAYASHI and K. KUWAHARA, *Appl. Surf. Sci.* **33/34** (1989) 594.
8. A. CATALANO, V. DALAL, E. A. FAGEN, R. B. HALL, J. V. MASI, J. D. MEAKIN, G. WARFIELD and A. M. BARNETT, in Proceedings of the International Conference on Photovoltaic Solar Energy, Luxembourg (Elsevier, Amsterdam, 1977) p. 644.
9. A. CATALANO, V. DALAL, W. E. DEVANCY, E. A. FAGEN, R. B. HALL, J. V. MASI, J. D. MEAKIN, G. WARFIELD, N. C. WYETH and A. M. BARNETT, Solar Energy Conference, Berlin (Commission of European Communities, Brussels, 1979) p. 328.

10. H. ABUSHAN and A. CATALANO, *Appl. Phys. Lett.* **38** (1980) 39.
11. P. S. NAYER and A. CATALANO, *ibid.* **39** (1981) 105.
12. K. R. MURALI and D. R. RAO, *J. Mater. Sci.* **16** (1981) 547.
13. *Idem, J. Mater. Sci. Lett.* **1** (1982) 383.
14. V. J. RAO, M. V. SALVI, V. SAMUEL and A. P. B. SINHA, *J . Mater. Sci.* **20** (1985) 3277.
15. J. L. DEISS, B. ELI-DRISSI, M. ROBINO and R. WEIL, *Appl. Phys. Lett.* **49** (1986) 969.
16. C. J. ARSENAULT and D. E. BRODIE, *Can. J. Phys.* **65** (1987) 756.
17. *Idem, ibid.* **66** (198) 373.
18. J. L. DEISS, B. ELI-DRISSI, M. ROBINO, M. TAPIRO, J. P. ZIELINGER and R. WEIL, *Physica Scripta* **37** (1988) 587.
19. P. LECANTE, A. MOSSET and J. GALY, *J. Appl. Cryst.* **18** (1985) 214.
20. D. M. NORTH and C. N. J. WAGNER, *ibid.* **2** (1969) 149.
21. F. HAJDU and G. PALINKAS, *ibid.* **5** (1972) 395.
22. G. HERMS and F. HAJDU, *ibid.* **17** (1984) 140.
23. C. N. J. WAGNER, *J. Non-Cryst. Solids* **31** (1978) 1.
24. International Tables for X-Ray Crystallography, Vol III, (Kynoch Press, Birmingham, 1969) pp. 59, 137.
25. A. BURIAN, P. LECANTE, A. MOSSET, J. GALY, J. VAN DUN and W. J. MORTIER, *J. Appl. Cryst.* **18** (1985) 487.
26. D. T. CROMER and J. T. WABER, *Acta Cryst.* **18** (1965) 104.
27. D. T. CROMER, *ibid.* **18** (1965) 17.
28. D. T. CROMER and J. B. MANN, *J. Chem. Phys.* **47** (1967) 1892.
29. C. W. DWIGGINS and D. A. PARK, *Acta Cryst.* **A27** (1971) 264.
30. C. W. DWIGGINS, *ibid.* **A28** (1972) 158.
31. B. E. WARREN and R. L. MOZZI, *ibid.* **21** (1966) 459.
32. G. MALET, C. CABOS, A. ESCANDE and P. DELORD, *J. Appl. Cryst.* **6** (1972) 139.
33. J. KROGH-MOE, *Acta Cryst.* **9** (1956) 951.
34. N. NORMAN, *ibid.* **10** (1957) 370.
35. A. BURIAN, P. LECANTE, A. MOSSET and J. GALY, *Z. Kristallogr.* **193** (1990) 199.
36. G. R. MICHELL, *Acta Cryst.* **A37** (1981) 488.
37. A. M. HINDELEH and R. HOSEMANN, *J. Phys. C (Solid State Phys.)* **21** (1988) 4155.
38. R. HOSEMANN, M. P. HENTSCHEL, F. J. BALTA-CALEJA, E. LOPEZ CABARCOS and A. M. HINDELEH, *J. Phys. C (Solid State Phys.)* **18** (1985) 961.
39. J. P. SUCHET, *J. Phys. Chem. Solids* **16** (1960) 265.
40. H. KREBS, *J. Non-Cryst. Solids* **1** (1969) 455.
41. G. LUCOVSKY and R. M. WHITE, *Phys. Rev.* **B8** (1973) 660.
42. J. S. KASPER and S. M. RICHARDS, *Acta Cryst.* **17** (1964) 752.
43. J. B. CLARK and K. J. RANGE, *Z. Naturforsch.* **31b** (1976) 158.
44. L. CERVINKA and A. HRUBY, *Acta Cryst.* **B26** (1970) 457.
45. J. HORN and K. LUKASZEWICZ, *Rocz. Chemii, Ann. Soc. Chim. Polonorum* **42** (1968) 933.
46. I. J. HEGYI, E. E. LOEBNER, E. W. POOR and J. G. WHITE, *Phys. Chem. Solids* **24** (1963) 333.
47. J. G. WHITE, *Acta Cryst.* **18** (1965) 217.
48. R. HOSEMANN, *Phys. Scripta* **T1** (1982) 142.
49. R. HOSEMANN, M. P. HENTSCHEL, A. LANGE and B. UTHER, *Z. Kristallogr.* **169** (1984) 13.
50. R. HOSEMANN and S. N. BAGCHI, in "Direct Analysis of Diffraction by Matter" (North-Holland, Amsterdam, 1962) p. 69.
51. S. N. BAGCHI, *Adv. Phys.* **19** (1970) 119.
52. S. N. BAGCHI, *Acta Cryst.* **A28** (1972) 560.

Received 25 February
and accepted 1 July 1991